*mathematics*

MDPI

*Article*

# Gamma-Distributed Memory and Hopf Stabilization in a Tumor–Macrophage Interaction Model

**Carlo Bianca [1,*], Luca Guerrini [2] and Stefania Ragni [3]**

[1] Efrei Research Lab, Université Paris-Panthéon-Assas, 30/32 Avenue de la République, 94800 Villejuif, France
[2] Department of Management, Polytechnic University of Marche, Piazzale Martelli 8, 60121 Ancona, Italy; luca.guerrini@univpm.it
[3] Department of Economics and Management, University of Ferrara, Via Voltapaletto 11, 44121 Ferrara, Italy; stefania.ragni@unife.it
* Correspondence: carlo.bianca@efrei.fr

## Abstract

Maturation and signaling in tumor-associated macrophages are distributed over time rather than concentrated at a single instant. We replace the discrete maturation lag in a tumor–macrophage model with weak and strong gamma memory kernels. Because the kernels are normalized, the equilibria of the original model are preserved, whereas the linear chain trick yields distinct polynomial characteristic equations for the two memory shapes. The analysis identifies kernel-dependent local stability thresholds for the coexistence equilibrium and shows that the same memory scale can correspond to different local regimes under weak and strong memory. We establish simple imaginary-axis crossings and verify transversality, so the results identify local Hopf thresholds. Sensitivity and two-parameter stability diagrams further describe how these thresholds depend on M2 growth, phenotype conversion and M2 loss.

**Keywords:** tumor–macrophage model; gamma distributed delay; Hopf bifurcation

**MSC:** 34K18; 37G15; 92C50

## 1. Introduction

Mathematical models of tumor–immune interactions are useful because they make explicit how tumor growth, immune activation and immune suppression compete over time [1–4]. In particular, tumor-associated macrophages (TAMs) play a dual role in cancer progression. Classically activated M1 macrophages are usually associated with pro-inflammatory and anti-tumor activity, whereas alternatively activated M2 macrophages promote angiogenesis, immunosuppression and metastasis [5–8]. The relative balance of these two phenotypes and the rate at which one is reprogrammed into the other are now widely viewed as central determinants of clinical outcome [7,8], and a substantial body of recent biological work focuses on therapeutic strategies that target this balance. The biological distinction between the two phenotypes is the basis of the tumor–macrophage model proposed by Shu et al. [1], which has motivated a sequence of further mathematical investigations [9–11]. Spatially structured and kinetic refinements have also been considered, including spatio-temporal multiphase models of the M1/M2 interplay [11], stochastic and deterministic kinetic descriptions of cancer–immune competition [12], and



Academic Editor: Zhouchao Wei

Received: 9 June 2026
Revised: 25 June 2026
Accepted: 29 June 2026
Published: 3 July 2026

kinetic derivations of cross-diffusion macroscopic equations from microscopic immune cell interactions [13].

Time delay is also important in tumor–immune dynamics because activation, differentiation, transport and maturation are not instantaneous [2–4,14–18]. Several tumor and immune models show that delays may change stability, generate oscillations, or produce more complicated long-time behavior such as bistability, multiple Hopf transitions, or chaotic regimes [2,9,19–22]. In the tumor–macrophage setting, recent work has incorporated polarization delay between M0 resting macrophages and the M1/M2 effector populations [10], M2 re-polarization delay as an immunotherapeutic mechanism [9], and combinations of multiple delays into a single tumor–immune system [19,23]. The delayed model of Dehingia et al. [24], which is the starting point of the present work, introduced a discrete time lag in the growth of pro-tumor M2 macrophages. In that model the delayed term is $x(t-\theta)z(t-\theta)$, so the present growth of M2 macrophages depends on the tumor–M2 interaction at one single past instant. A second line of work [25] similarly investigated discrete-delay effects in a related tumor–immune–normal cell model and confirmed that the delay can both destabilize an otherwise stable equilibrium and stabilize an otherwise unstable one.

The fixed-delay assumption is mathematically convenient but biologically restrictive. In a heterogeneous cellular population, maturation times, transit times across compartments and cytokine production times are distributed rather than identical [26–29]. Distributed delays provide a standard way to model this heterogeneity and are widely used in biological and population dynamics; recent contributions have analyzed the convergence rate of the linear chain trick [30], derived equivalences between distributed-delay differential equations and compartmental ODE models [27], designed hypoexponential approximations of gamma-distributed delays for accurate numerical simulation [28], and generalized the chain trick to broader phase-type distributions [26]. Stability and Hopf bifurcation under generic delay distribution kernels have been studied in single-species logistic models [31], in nonlinear delay differential models of biological network motifs [32], and through oscillatory time-history kernels relevant to disease dynamics [29]. Recent tumor-control work also illustrates how memory and nonlocal temporal mechanisms can change stability regimes [33]; broader nonlinear-network studies provide complementary methodological perspective [34]. Within the tumor–immune literature, continuously distributed delays have been used to model immune activation and CD8+ T cell recruitment [16], and re-polarization delays of pro-tumor macrophages have been investigated as an immunotherapy mechanism [9]. Earlier theoretical foundations for distributed-delay analysis remain essential and are due to MacDonald [35], Cushing [36], Kuang [37], Hale and Verduyn Lunel [38], Smith [39], Ruan [40], and Bellman and Cooke [41], with the normal-form analysis used to characterize Hopf bifurcations traceable to Hassard, Kazarinoff and Wan [42]. Related delayed cellular dynamics with similar mathematical structure have been studied for HTLV-I infection [43], while classical low-dimensional ODE descriptions of the tumor–effector–cytokine interplay continue to provide a reference framework for delayed and distributed-memory extensions [44].

The aim of the present paper is to move beyond the point-delay assumption of Dehingia et al. [24] and to examine how the shape of the maturation memory affects the local dynamics of the same tumor–macrophage interaction mechanism. To this end, we replace the delayed product by two normalized gamma kernels. The weak kernel describes exponentially fading memory, in which recent tumor–M2 interactions have the greatest influence, whereas the strong kernel describes a peaking memory with an effective maturation period before past interactions exert their largest effect. Because both kernels have unit mass, the replacement preserves the equilibria of the reference model; at the same time, the

linear chain trick converts the two distributed-memory formulations into finite-dimensional ordinary differential systems, making their local stability accessible through polynomial characteristic equations and the Routh–Hurwitz criterion. This formulation makes it possible to isolate the effect of memory shape without changing either the underlying biological interactions or the equilibrium structure. Although the two gamma kernels are calibrated through the same memory-scale parameter, they distribute the influence of past tumor–M2 interactions differently and may therefore lead to different local stability boundaries. For the reference parameter set, the two kernels place the same representative memory scale on opposite sides of their respective stability boundaries, even though their threshold mean memories are close. Thus, the relevant distinction is not simply the average duration of memory, but also how that memory is distributed over time; this regime difference cannot be inferred from a fixed-delay description alone. The results concern local dynamics near the coexistence equilibrium. More precisely, we identify spectral stability thresholds and verify transverse crossings of a simple imaginary pair. Hence, when a threshold is crossed, small perturbations change from decaying oscillations to oscillations whose linearized amplitude grows. This is a local mathematical conclusion, not a clinical prediction. We do not compute the first Lyapunov coefficient, continue nonlinear periodic orbits, or establish global stability; these questions are consequently left as explicit limitations and directions for future work.

This paper is organized as follows. Section 2 recalls the reference model and introduces the distributed-memory extension. Section 3 derives the weak and strong chain systems. Section 4 proves that the equilibria are unchanged. Section 5 derives the characteristic equations in detail, starting from the augmented Jacobian and obtaining the rational kernel factor by direct computation. Sections 6 and 7 give the Routh–Hurwitz stability calculations and the resulting Hopf conditions. Section 8 compares the thresholds and the numerical solutions through compact figure captions and a quantitative comparison against the reference discrete-delay paper. Section 9 discusses the biological interpretation and the modeling consequences.

## 2. Reference Model and Distributed-Delay Extension

The nondimensional delayed tumor–macrophage model studied in the reference paper [24] is

$$\begin{cases} \dfrac{dx}{dt} = \alpha x(1-\beta x) - \delta xy + \eta xz, \\ \dfrac{dy}{dt} = xy - \mu_1 y - \gamma_1 y + \gamma_2 z, \\ \dfrac{dz}{dt} = \xi\, x(t-\theta)z(t-\theta) - \mu_2 z + \gamma_1 y - \gamma_2 z. \end{cases} \tag{1}$$

Here, $x$, $y$ and $z$ denote, respectively, tumor cells, anti-tumor M1 macrophages and pro-tumor M2 macrophages. The parameter $\theta$ is the discrete delay in the pro-tumor M2 growth process. All parameters are non-negative. We replace the discrete delayed product in (1) by a distributed memory. The resulting model is

$$\begin{cases} \dfrac{dx}{dt} = \alpha x(1-\beta x) - \delta xy + \eta xz, \\ \dfrac{dy}{dt} = xy - \mu_1 y - \gamma_1 y + \gamma_2 z, \\ \dfrac{dz}{dt} = \xi \displaystyle\int_0^\infty K_T(s)\, x(t-s)z(t-s)\, ds - \mu_2 z + \gamma_1 y - \gamma_2 z. \end{cases} \tag{2}$$

where $K_T \geq 0$ and

$$\int_0^\infty K_T(s)\, ds = 1.$$

We consider the two gamma kernels

$$K_T^w(s) = \frac{1}{T}e^{-s/T}, \qquad K_T^s(s) = \frac{s}{T^2}e^{-s/T}, \qquad s \geq 0.$$

The weak kernel gives greatest weight to recent tumor–M2 interactions. By contrast, the strong kernel vanishes at the present time, reaches its maximum after a positive maturation time and subsequently decays. Their Laplace transforms are

$$\widehat{K}_T^w(\lambda) = \frac{1}{1+T\lambda}, \qquad \widehat{K}_T^s(\lambda) = \frac{1}{(1+T\lambda)^2}.$$

Thus, the weak kernel has mean memory $T$, whereas the strong kernel has mean memory $2T$; in the latter case, $T$ is a scale parameter rather than the mean memory. Figure 1 summarizes the biological interactions retained in both the discrete-delay and distributed-memory formulations. Table 1 lists the parameters and the baseline values used in the numerical analysis.

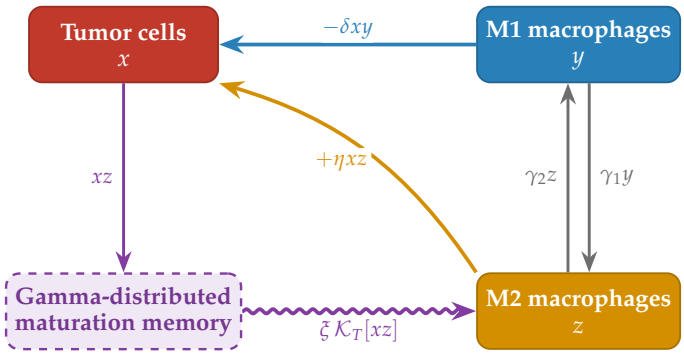


**Figure 1.** Schematic of the tumor–macrophage interactions. Tumor cells are inhibited by M1 macrophages through the term $-\delta xy$ and promoted by M2 macrophages through the term $+\eta xz$. The two macrophage phenotypes interconvert at rates $\gamma_1$ and $\gamma_2$. The M2 growth input is determined by the normalized gamma-weighted history $\mathcal{K}_T[xz]$ of the tumor–M2 interaction, processed through the distributed maturation memory.

**Table 1.** Model parameters, roles and baseline values used in the numerical analysis.

| Parameter | Mathematical Role | Biological Interpretation | Value |
|---|---|---|---|
| $\alpha$ | tumor growth coefficient | intrinsic tumor growth | 0.565 |
| $\beta$ | tumor self-limitation | inverse carrying-capacity scale | 0.002 |
| $\delta$ | $xy$ interaction coefficient | M1-mediated tumor inhibition | 2 |
| $\eta$ | $xz$ interaction coefficient | M2-mediated tumor promotion | 0.1 |
| $\mu_1, \mu_2$ | loss rates | M1 and M2 removal/death | 0.2, 0.2 |
| $\xi$ | delayed-product coefficient | M2 growth induced by tumor–M2 interaction | 1.05 |
| $\gamma_1, \gamma_2$ | conversion coefficients | M1-to-M2 and M2-to-M1 conversion | 0.05, 0.04 |
| $T$ | memory scale | scale of gamma maturation distribution | variable |

## 3. Linear Chain Formulation

Starting from the distributed model (2), for the weak kernel define the auxiliary variable

$$w(t) = \int_0^\infty \frac{1}{T}e^{-s/T}x(t-s)z(t-s)\,ds.$$

Assuming the standard regularity and boundedness needed for differentiating under the integral sign, write $u(t) = x(t)z(t)$. Since $\partial_t u(t-s) = -\partial_s u(t-s)$, integration by parts gives

$$\frac{dw}{dt} = -\int_0^\infty \frac{1}{T} e^{-s/T} \partial_s u(t-s)\, ds = \frac{u(t)}{T} - \int_0^\infty \frac{1}{T^2} e^{-s/T} u(t-s)\, ds = \frac{x(t)z(t) - w(t)}{T}.$$

Therefore, the weak gamma model is the four-dimensional system

$$\begin{cases} \dfrac{dx}{dt} = \alpha x(1-\beta x) - \delta xy + \eta xz, \\ \dfrac{dy}{dt} = xy - \mu_1 y - \gamma_1 y + \gamma_2 z, \\ \dfrac{dz}{dt} = \xi w - \mu_2 z + \gamma_1 y - \gamma_2 z, \\ \dfrac{dw}{dt} = \dfrac{xz - w}{T}. \end{cases} \tag{3}$$

For the strong kernel, introduce the two auxiliary variables

$$v(t) = \int_0^\infty \frac{1}{T} e^{-s/T} x(t-s)z(t-s)\, ds, \qquad w(t) = \int_0^\infty \frac{s}{T^2} e^{-s/T} x(t-s)z(t-s)\, ds.$$

Differentiating $v$ as before gives $dv/dt = (xz - v)/T$, while differentiating $w$ and using integration by parts gives

$$\frac{dw}{dt} = \int_0^\infty \frac{1}{T^2} e^{-s/T} x(t-s)z(t-s)\, ds - \int_0^\infty \frac{s}{T^3} e^{-s/T} x(t-s)z(t-s)\, ds = \frac{v - w}{T}.$$

Hence, the strong gamma model is

$$\begin{cases} \dfrac{dx}{dt} = \alpha x(1-\beta x) - \delta xy + \eta xz, \\ \dfrac{dy}{dt} = xy - \mu_1 y - \gamma_1 y + \gamma_2 z, \\ \dfrac{dz}{dt} = \xi w - \mu_2 z + \gamma_1 y - \gamma_2 z, \\ \dfrac{dv}{dt} = \dfrac{xz - v}{T}, \\ \dfrac{dw}{dt} = \dfrac{v - w}{T}. \end{cases} \tag{4}$$

We stress that in the strong chain, $w$ is the integral against $K_T^s$ and not against $K_T^w$.

## 4. Equilibria

**Proposition 1.** *The equilibria of the distributed-memory systems* (3) *and* (4) *have the same* $(x, y, z)$*-coordinates as the equilibria of the discrete-delay model* (1)*.*

**Proof.** At equilibrium all state variables are constant in time. Let $(x^*, y^*, z^*)$ be a constant solution of the $(x, y, z)$-subsystem. The history is then $x(t-s)z(t-s) = x^*z^*$ for every $s \geq 0$. Since both kernels have unit mass,

$$\int_0^\infty K_T(s)\, x^*z^*\, ds = x^*z^* \int_0^\infty K_T(s)\, ds = x^*z^*,$$

so the distributed term in (2) reduces to $\xi x^*z^*$, which is exactly the right-hand side that appears in the nondelayed model. Hence, the three algebraic equilibrium equations coincide with those of (1) for any $\theta$, including $\theta = 0$. The memory variables are determined by the chain equations: from $dw/dt = 0$ in (3) we obtain $w^* = x^*z^*$, and from $dv/dt = 0$ and $dw/dt = 0$ in (4) we obtain $v^* = w^* = x^*z^*$. Hence, the augmented equilibria are uniquely determined by the $(x, y, z)$-coordinates of any equilibrium of (1). □

The equilibria are

$$E_0 = (0,0,0), \qquad E_1 = \left(\frac{1}{\beta},0,0\right), \qquad E^* = (x^*,y^*,z^*).$$

The first two are obtained by inspection: in $E_0$ all populations vanish, and in $E_1$ the tumor is at carrying capacity $1/\beta$ while both macrophage populations are absent. To compute the coexistence equilibrium $E^*$, we add the second and third equations of (1) at steady state. The cross-terms in $\gamma_1$ and $\gamma_2$ cancel, giving $(x^* - \mu_1)y^* + (\xi x^* - \mu_2)z^* = 0$, while the second equation alone gives $(x^* - \mu_1 - \gamma_1)y^* + \gamma_2 z^* = 0$. Eliminating $y^*$ and $z^*$ via these two linear relations and using the first equation $\alpha(1-\beta x^*) - \delta y^* + \eta z^* = 0$ leads, after some algebra, to a single quadratic in $x^*$:

$$\xi(x^*)^2 - (\xi\mu_1 + \xi\gamma_1 + \mu_2 + \gamma_2)\, x^* + (\mu_1\mu_2 + \mu_1\gamma_2 + \mu_2\gamma_1) = 0,$$

with

$$y^* = \frac{\alpha(1-\beta x^*)\gamma_2}{\delta\gamma_2 + \eta(x^* - \mu_1 - \gamma_1)}, \qquad z^* = \frac{\alpha(1-\beta x^*)(\mu_1 + \gamma_1 - x^*)}{\delta\gamma_2 + \eta(x^* - \mu_1 - \gamma_1)}.$$

For biological feasibility, one requires $x^* > 0$, $y^* > 0$, $z^* > 0$.

**Remark 1.** *Two algebraic identities, valid at $E^*$, will be used repeatedly:*

$$\alpha\beta x^* + \delta y^* = \alpha + \eta z^*, \qquad x^* - \mu_1 - \gamma_1 = -\frac{\gamma_2 z^*}{y^*}.$$

*The first follows directly from $\alpha(1-\beta x^*) - \delta y^* + \eta z^* = 0$, namely $\alpha - \alpha\beta x^* - \delta y^* + \eta z^* = 0$, after rearrangement; the second is the second equation of (1) at equilibrium divided by $y^* \neq 0$. These identities simplify the entries of the Jacobian below.*

**Proposition 2** (Positive invariance of the chain systems)**.** *For nonnegative initial data, the non-negative orthant is positively invariant for the weak and strong chain systems (3) and (4).*

**Proof.** On $x = 0$, the first right-hand side is zero; on $y = 0$ it equals $\gamma_2 z \geq 0$; and on $z = 0$ it equals $\xi w + \gamma_1 y \geq 0$. In the weak system, on $w = 0$ one has $w' = xz/T \geq 0$. In the strong system, on $v = 0$ one has $v' = xz/T \geq 0$, and on $w = 0$ one has $w' = v/T \geq 0$. Hence, the vector field points inward on every coordinate face. □

This result does not by itself provide boundedness or global asymptotic stability. The present paper is restricted to local dynamics near $E^*$; a global analysis is left for future work.

## 5. Linearization and Characteristic Equations

We now linearize the augmented systems at $E^*$ in order to derive the characteristic equations that will be used in the subsequent Routh–Hurwitz analysis. Set

$$x(t) = x^* + X(t), \qquad y(t) = y^* + Y(t), \qquad z(t) = z^* + Z(t),$$

and analogously introduce perturbations of the auxiliary memory variables in the weak and strong chain systems.

A direct computation of the partial derivatives gives

$$\frac{\partial}{\partial x}\Big(\alpha x(1-\beta x) - \delta xy + \eta xz\Big)\Big|_{E^*} = \alpha - 2\alpha\beta x^* - \delta y^* + \eta z^*.$$

Using the first equilibrium identity,

$$\alpha - \alpha\beta x^* - \delta y^* + \eta z^* = 0,$$

this entry reduces to $-\alpha\beta x^*$. The remaining first-row entries are $-\delta x^*$ and $\eta x^*$. The second row gives $y^*$, $x^* - \mu_1 - \gamma_1$ and $\gamma_2$, and the second equilibrium identity yields

$$x^* - \mu_1 - \gamma_1 = -\frac{\gamma_2 z^*}{y^*}.$$

Therefore, the instantaneous part of the linearized $(x, y, z)$-system is

$$A = \begin{pmatrix} -\alpha\beta x^* & -\delta x^* & \eta x^* \\ y^* & -\dfrac{\gamma_2 z^*}{y^*} & \gamma_2 \\ 0 & \gamma_1 & -(\mu_2 + \gamma_2) \end{pmatrix}.$$

The product inside the delayed or distributed feedback term has the linearization

$$x(t-s)z(t-s) = x^* z^* + x^* Z(t-s) + z^* X(t-s) + \text{higher-order terms.}$$

For the discrete-delay model (1), the linearized third equation therefore contains the contribution

$$\xi\big(z^* X(t-\theta) + x^* Z(t-\theta)\big).$$

Seeking solutions of the form

$$(X, Y, Z) = (X_0, Y_0, Z_0)e^{\lambda t},$$

gives the characteristic equation

$$P(\lambda) + e^{-\lambda\theta} Q(\lambda) = 0, \tag{5}$$

where

$$P(\lambda) = \det(\lambda I - A) = \lambda^3 + p_1\lambda^2 + p_2\lambda + p_3, \qquad Q(\lambda) = q_1\lambda^2 + q_2\lambda + q_3.$$

Expanding $\det(\lambda I - A)$ and using the equilibrium identities gives

$$\begin{aligned} p_1 &= \alpha\beta x^* + \mu_2 + \gamma_2 + \frac{\gamma_2 z^*}{y^*}, \\ p_2 &= \alpha\beta x^* \left(\mu_2 + \gamma_2 + \frac{\gamma_2 z^*}{y^*}\right) + (\mu_2 + \gamma_2)\frac{\gamma_2 z^*}{y^*} + \delta x^* y^* - \gamma_1\gamma_2, \\ p_3 &= (\mu_2 + \gamma_2)\left(\frac{\gamma_2 z^*}{y^*}\alpha\beta x^* + \delta x^* y^*\right) - \alpha\beta\gamma_1\gamma_2 x^* - \gamma_1\eta x^* y^*. \end{aligned}$$

Similarly, the coefficients associated with the delayed feedback are

$$\begin{aligned} q_1 &= -\xi x^*, \\ q_2 &= -\xi x^* \left(\frac{\gamma_2 z^*}{y^*} + \alpha\beta x^* + \eta z^*\right), \\ q_3 &= -\xi x^* \left[\frac{\gamma_2 z^*}{y^*}\alpha\beta x^* + \delta x^* y^* + z^*\left(\eta\frac{\gamma_2 z^*}{y^*} - \delta\gamma_2\right)\right]. \end{aligned}$$

For the distributed-delay model, the linearized convolution term becomes

$$\widehat{K_T}(\lambda)\big(z^* X_0 + x^* Z_0\big)e^{\lambda t},$$

where $\widehat{K_T}$ is the Laplace transform of the memory kernel. Consequently, the characteristic equation takes the form

$$P(\lambda) + \widehat{K_T}(\lambda)Q(\lambda) = 0. \tag{6}$$

Thus, for the weak and strong gamma kernels, respectively, one obtains

$$P(\lambda) + \frac{1}{1+T\lambda}Q(\lambda) = 0 \tag{7}$$

and

$$P(\lambda) + \frac{1}{(1+T\lambda)^2}Q(\lambda) = 0. \tag{8}$$

The relations (7) and (8) give a compact description of the local spectrum. To apply the Routh–Hurwitz criterion, we now derive explicitly the polynomial characteristic equations of the finite-dimensional weak and strong chain systems. These calculations lead directly to the quartic and quintic polynomials used in the following stability analysis. For the weak kernel, the Jacobian of the four-dimensional chain system at $E^*$ is

$$J_w = \begin{pmatrix} -\alpha\beta x^* & -\delta x^* & \eta x^* & 0 \\ y^* & -\gamma_2 z^*/y^* & \gamma_2 & 0 \\ 0 & \gamma_1 & -(\mu_2+\gamma_2) & \xi \\ z^*/T & 0 & x^*/T & -1/T \end{pmatrix}.$$

Let $D_w(\lambda) = \det(\lambda I - J_w)$. Expanding along the last column gives

$$D_w(\lambda) = \left(\lambda + \frac{1}{T}\right)M_{44}(\lambda) + \xi M_{34}(\lambda).$$

Using the equilibrium identities and evaluating the two minors yields

$$M_{44}(\lambda) = P(\lambda), \qquad \xi M_{34}(\lambda) = \frac{Q(\lambda)}{T}.$$

Hence,

$$D_w(\lambda) = \frac{1}{T}[(1+T\lambda)P(\lambda) + Q(\lambda)].$$

Therefore, the weak-chain characteristic equation is

$$(1+T\lambda)P(\lambda) + Q(\lambda) = 0.$$

After expansion, this gives the quartic polynomial analyzed in Section 6. For the strong kernel, let $w_1$ and $w_2$ be the two memory variables, where $w_2$ enters the equation for the M2 population. At coexistence,

$$w_1^* = w_2^* = x^* z^*.$$

With the ordering $(x, y, z, w_1, w_2)$, the Jacobian is

$$J_s = \begin{pmatrix} A & 0 & b \\ c^\top/T & -1/T & 0 \\ 0^\top & 1/T & -1/T \end{pmatrix}, \qquad b = \begin{pmatrix} 0 \\ 0 \\ \xi \end{pmatrix}, \qquad c = \begin{pmatrix} z^* \\ 0 \\ x^* \end{pmatrix}.$$

Successive expansion along the two chain-variable columns gives

$$\det(\lambda I - J_s) = \frac{1}{T^2}\Big[(1+T\lambda)^2 P(\lambda) + Q(\lambda)\Big].$$

Thus, the strong-chain characteristic equation is

$$(1 + T\lambda)^2 P(\lambda) + Q(\lambda) = 0.$$

Its expansion gives the quintic polynomial analyzed in Section 7. The different polynomial degrees arise because the weak kernel is represented by one memory stage, whereas the strong kernel requires two consecutive memory stages.

## 6. Weak Gamma Stability Calculation

Multiplying (7) by $1 + T\lambda$ gives

$$T\lambda^4 + (1 + p_1 T)\lambda^3 + (p_1 + q_1 + p_2 T)\lambda^2 + (p_2 + q_2 + p_3 T)\lambda + (p_3 + q_3) = 0. \quad (9)$$

This is a genuine quartic in $\lambda$ as long as $T > 0$. Dividing by $T$, write (9) as

$$\lambda^4 + a_1\lambda^3 + a_2\lambda^2 + a_3\lambda + a_4 = 0,$$

where

$$a_1 = \frac{1 + p_1 T}{T}, \quad a_2 = \frac{p_1 + q_1 + p_2 T}{T}, \quad a_3 = \frac{p_2 + q_2 + p_3 T}{T}, \quad a_4 = \frac{p_3 + q_3}{T}.$$

For a real-coefficient quartic, the Routh–Hurwitz criterion can be stated through the leading principal minors of the Hurwitz matrix

$$H_4 = \begin{pmatrix} a_1 & a_3 & 0 & 0 \\ 1 & a_2 & a_4 & 0 \\ 0 & a_1 & a_3 & 0 \\ 0 & 1 & a_2 & a_4 \end{pmatrix},$$

whose leading minors are $\Delta_1 = a_1$, $\Delta_2 = a_1 a_2 - a_3$, $\Delta_3 = a_3\Delta_2 - a_1^2 a_4 = a_1 a_2 a_3 - a_3^2 - a_1^2 a_4$, and $\Delta_4 = a_4\Delta_3$. Local asymptotic stability is equivalent to $\Delta_j > 0$ for $j = 1, \ldots, 4$. Since $\Delta_4 = a_4\Delta_3$, the four positivity conditions reduce to

$$a_1 > 0, \quad a_2 > 0, \quad a_3 > 0, \quad a_4 > 0, \quad a_1 a_2 a_3 > a_3^2 + a_1^2 a_4. \quad (10)$$

For the parameter set used in Section 8, the first four inequalities remain positive near the transition. The fifth condition is the active stability condition that selects the relevant boundary; as $T$ varies, it is the one that fails first under our parameter set. The Hopf boundary is obtained by replacing the last inequality in (10) by equality, while the four positivity conditions remain valid, so the polynomial has a pair of pure-imaginary roots $\lambda = \pm i\omega_w$ and the remaining roots have negative real parts. Setting $\lambda = i\omega_w$ in (9) and separating real and imaginary parts gives the two equations $\omega_w^4 - a_2\omega_w^2 + a_4 = 0$ and $a_3\omega_w^2 = a_1\omega_w^4$, i.e., $\omega_w^2 = a_3/a_1$; substituting back gives

$$a_1 a_2 a_3 = a_3^2 + a_1^2 a_4. \quad (11)$$

This is the algebraic equation that determines $T_{c,w}$.

**Remark 2.** *By Liu's criterion [45] for a real-coefficient polynomial with a simple pair of pure-imaginary roots, the transversality condition* $\frac{d}{dT}\mathrm{Re}\,\lambda(T) \neq 0$ *at* $T = T_{c,w}$ *is equivalent to*

$$\left.\frac{d\Delta_3}{dT}\right|_{T=T_{c,w}} \neq 0,$$

*where* $\Delta_3 = a_1a_2a_3 - a_3^2 - a_1^2a_4$ *is the Hurwitz determinant defined above. The sign of the derivative determines the direction of the crossing. We verify both the non-vanishing and the (negative) sign of* $d\Delta_3/dT$ *numerically in Section 8, where the corresponding rate of change of* $\mathrm{Re}\,\lambda$ *is also reported.*

## 7. Strong Gamma Stability Calculation

Multiplying (8) by $(1+T\lambda)^2$ gives

$$\begin{aligned} &T^2\lambda^5 + (p_1T^2 + 2T)\lambda^4 + (p_2T^2 + 2p_1T + 1)\lambda^3 \\ &\quad + (p_3T^2 + 2p_2T + p_1 + q_1)\lambda^2 + (2p_3T + p_2 + q_2)\lambda + (p_3 + q_3) = 0. \end{aligned} \tag{12}$$

After division by $T^2$, write (12) as

$$\lambda^5 + b_1\lambda^4 + b_2\lambda^3 + b_3\lambda^2 + b_4\lambda + b_5 = 0,$$

where

$$\begin{aligned} b_1 &= \frac{p_1T^2 + 2T}{T^2}, \quad b_2 = \frac{p_2T^2 + 2p_1T + 1}{T^2}, \\ b_3 &= \frac{p_3T^2 + 2p_2T + p_1 + q_1}{T^2}, \quad b_4 = \frac{2p_3T + p_2 + q_2}{T^2}, \quad b_5 = \frac{p_3 + q_3}{T^2}. \end{aligned}$$

The Routh–Hurwitz criterion for a real-coefficient quintic is expressed through the principal minors $\Delta_j$, $j = 1, \ldots, 5$, of the Hurwitz matrix

$$H_5 = \begin{pmatrix} b_1 & b_3 & b_5 & 0 & 0 \\ 1 & b_2 & b_4 & 0 & 0 \\ 0 & b_1 & b_3 & b_5 & 0 \\ 0 & 1 & b_2 & b_4 & 0 \\ 0 & 0 & b_1 & b_3 & b_5 \end{pmatrix},$$

namely $\Delta_1 = b_1$, $\Delta_2 = b_1b_2 - b_3$, $\Delta_3 = b_3\Delta_2 - b_1(b_1b_4 - b_5) = b_1b_2b_3 - b_3^2 - b_1^2b_4 + b_1b_5$, $\Delta_4$ as below, and $\Delta_5 = b_5\Delta_4$. The Routh–Hurwitz stability conditions are

$$\Delta_1 > 0, \quad \Delta_2 > 0, \quad \Delta_3 > 0, \quad \Delta_4 > 0, \quad \Delta_5 > 0.$$

Because $\Delta_5 = b_5\Delta_4$, the last two conditions are jointly equivalent to $b_5 > 0$ and $\Delta_4 > 0$. A simple Hopf boundary is therefore identified by

$$\Delta_4 = 0, \tag{13}$$

provided that $\Delta_1, \Delta_2, \Delta_3$ and $b_5$ remain strictly positive and the crossing pair of imaginary eigenvalues is simple. The Hurwitz determinant $\Delta_4$ can be written explicitly as

$$\Delta_4 = -b_1^2b_4^2 - b_1b_2^2b_5 + b_1b_2b_3b_4 + 2b_1b_4b_5 + b_2b_3b_5 - b_3^2b_4 - b_5^2.$$

Equivalently, using the expression for $\Delta_3$,

$$\Delta_4 = b_4\Delta_3 - b_5\Big(b_1b_2^2 - b_2b_3 - b_1b_4 + b_5\Big).$$

This is the algebraic equation solved numerically in Section 8 to obtain $T_{c,s}$. We remark that the condition $\Delta_5 > 0$ is strict away from the boundary: at the boundary, $\Delta_5$ vanishes because $\Delta_4$ does, which is why $\Delta_4 = 0$ alone (together with $b_5, \Delta_1, \Delta_2, \Delta_3 > 0$) is the correct Hopf identification. By the same Liu-type argument used in the quartic case [45], the

transversality condition $\frac{d}{dT}\mathrm{Re}\,\lambda(T) \neq 0$ at $T = T_{c,s}$ is equivalent to $\frac{d\Delta_4}{dT} \neq 0$, which we again verify numerically.

**Remark 3.** *The strong-kernel polynomial* (12) *reduces, in the formal limit* $T \to 0$, *to* $P(\lambda) + Q(\lambda) = 0$, *which is the characteristic equation of the nondelayed model* (1) *with* $\theta = 0$. *The same limit holds in* (9). *Thus, both distributed-delay models continuously connect with the instantaneous model, while the discrete-delay model recovers the same limit through the analytic limit* $e^{-\lambda\theta} \to 1$.

## 8. Numerical Local-Stability Analysis

All numerical stability boundaries below are computed from the eigenvalues of the augmented Jacobians associated with (3) and (4); the reported spectral abscissa is $\max_j \mathrm{Re}(\lambda_j)$. Time simulations use the common physical initial condition $(x(0), y(0), z(0)) = (2, 0.2, 0.4)$ and compatible chain initial values $w(0) = x(0)z(0)$ for the weak system and $v(0) = w(0) = x(0)z(0)$ for the strong system. The numerical diagrams are local linear-stability computations and are not a continuation of nonlinear periodic orbits. All computations were performed in Python 3.12. Eigenvalue and Hurwitz-determinant evaluations used numpy.linalg.eigvals; the Hopf threshold search used the bisection method applied to the relevant Hurwitz determinant ($\Delta_3$ for the quartic, $\Delta_4$ for the quintic) with tolerance $10^{-8}$. Time-domain simulations used `scipy.integrate.solve_ivp` with the explicit Runge–Kutta method of order 5(4) (Dormand–Prince, `method='RK45'`) and relative and absolute tolerances rtol = atol = $10^{-10}$, integrated over the interval $[0, 3000]$.

We use the parameter set of Dehingia et al. [24]:

$$\alpha = 0.565,\ \beta = 0.002,\ \delta = 2,\ \eta = 0.1,\ \mu_1 = \mu_2 = 0.2,\ \xi = 1.05,\ \gamma_1 = 0.05,\ \gamma_2 = 0.04.$$

For these values, the quadratic equation for $x^*$ has two positive roots, namely 0.28423 and 0.19435. The larger root gives $z^* < 0$ and is therefore not biologically feasible. The biologically admissible coexistence equilibrium is

$$E^* = (0.194346,\ 0.303504,\ 0.422279).$$

The corresponding coefficients in the characteristic equation are

$$p_1 = 0.295873, \quad p_2 = 0.129392, \quad p_3 = 0.028020,$$

$$q_1 = -0.204064, \quad q_2 = -0.020019, \quad q_3 = -0.017662.$$

In particular, $p_3 + q_3 = 0.010359 > 0$, so the constant terms of the weak and strong characteristic polynomials are positive for all $T > 0$. Solving the quartic Hopf condition (11) and the quintic condition (13), while checking the remaining Routh–Hurwitz inequalities, gives

$$T_{c,w} = 0.169409, \qquad T_{c,s} = 0.085863.$$

At both critical values the crossing is simple and stabilizing. Numerically, the slope of $\max_j \mathrm{Re}(\lambda_j)$ at the boundary is approximately $-8.14 \times 10^{-3}$ for the weak kernel and $-1.59 \times 10^{-2}$ for the strong kernel. Hence, the real part of the critical conjugate pair decreases through zero as $T$ increases; the transversality condition required for a Hopf crossing is therefore satisfied for the present parameter set.

The continuation curves show that the threshold is not a property of $T$ alone. Over the reported parameter ranges, increasing either conversion rate $\gamma_1$ or $\gamma_2$ shifts both weak- and strong-kernel thresholds upward, whereas increasing the M2 loss rate $\mu_2$

shifts them downward; the dependence on the delayed-product coefficient $\xi$ is also monotone. Thus, the kernel-shape effect persists under changes in M2 turnover and in both phenotype-conversion mechanisms, rather than being tied to a single parameter choice. The two-parameter diagrams complement these one-parameter continuations by tracing the local stability boundary in the $(\xi, T)$ plane. All curves should be interpreted as continuations of the local linear spectral boundary only; nonlinear branches of periodic solutions are beyond the present scope.

### *8.1. Quantitative Comparison with the Reference Fixed-Delay Model*

Table 2 is the key numerical comparison with the reference model [24]. The comparison can be read at three different levels, each of which carries a distinct modeling message.

**Table 2.** Comparison of the reference discrete delay [24] with the weak and strong gamma distributed delays. The last column reports the actual mean of the memory kernel.

| Model | Characteristic Factor | Critical Scale | Mean at Threshold |
|---|---|---|---|
| Discrete delay | $e^{-\lambda\theta}$ | $\theta_c \approx 0.205$ | 0.205 |
| Weak gamma | $(1+T\lambda)^{-1}$ | $T_{c,w} \approx 0.169409$ | 0.169409 |
| Strong gamma | $(1+T\lambda)^{-2}$ | $T_{c,s} \approx 0.085863$ | $2T_{c,s} \approx 0.171726$ |

(i) Critical scale parameter $T$. If $T$ is interpreted naively as the "delay" of the system, the two distributed models stabilize the coexistence equilibrium earlier than the discrete delay: $T_{c,w} \approx 0.169$ and $T_{c,s} \approx 0.086$, whereas $\theta_c \approx 0.205$. A purely numerical reading would conclude that the strong kernel is the fastest stabilizer, the weak kernel intermediate, and the discrete delay the slowest. As discussed below, this is the wrong comparison.

(ii) Mean memory at threshold. For the weak kernel the mean equals $T$, so $T_{c,w}$ is already the mean memory; for the strong kernel the mean equals $2T$, so the relevant mean is $2T_{c,s} \approx 0.172$. Once both kernels are compared on the basis of their mean memory, the two distributed thresholds are essentially indistinguishable, 0.169 versus 0.172, a relative difference of less than 2%. This shows that, for the present parameter set, the average amount of memory required to stabilize the coexistence equilibrium is, to a good approximation, the same for both kernel shapes. The visible difference in the scale-parameter values is therefore an artifact of the kernel parametrization, not a structural property of the dynamics.

(iii) Distributed versus discrete memory. Both distributed thresholds, however expressed (scale or mean), lie strictly below the discrete-delay threshold $\theta_c \approx 0.205$. For the reported parameter set, this indicates that replacing a point history by a distributed history changes the phase and gain of the linear feedback. Spectrally, the transcendental factor $e^{-\lambda\theta}$ in (5) is replaced by the rational factor $\widehat{K_T}(\lambda)$ in (6); this replacement shifts the local spectral boundary. We do not interpret the resulting numerical gap as a universal biological effect, but as a model-dependent consequence of the assumed memory shape.

### *8.2. Interpretation of the Local Stability Diagrams*

Figure 2 gives the requested bifurcation-style representation: the dominant real part crosses zero at $T_{c,s} = 0.085863$ for the strong kernel and at $T_{c,w} = 0.169409$ for the weak kernel. The crossing is transverse for the reference parameter set.

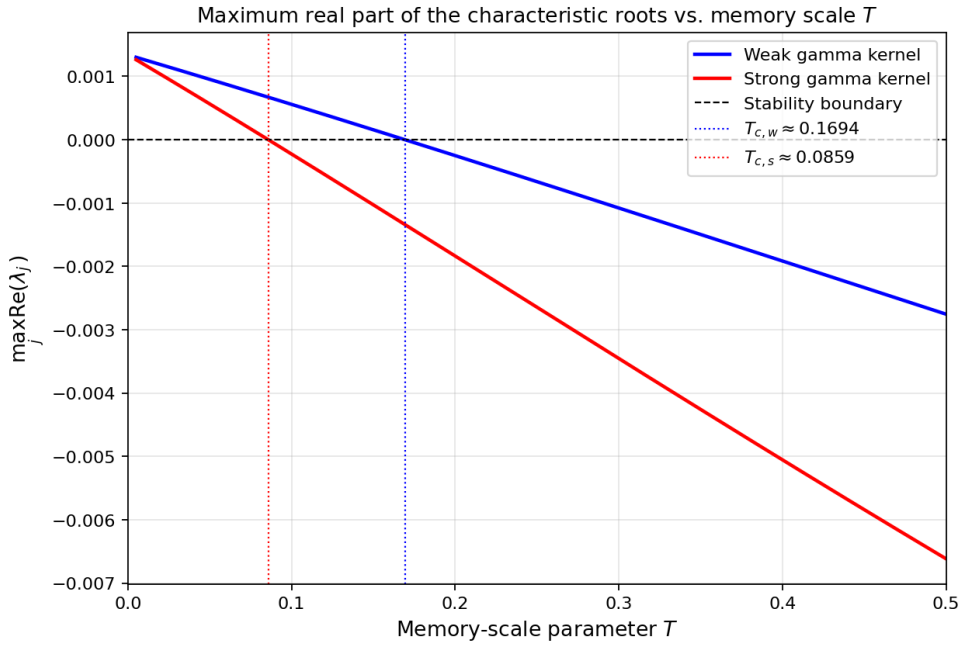


**Figure 2.** One-parameter local stability-bifurcation diagram. The vertical axis is the spectral abscissa $\max_j \mathrm{Re}(\lambda_j)$. The zero line separates unstable and locally asymptotically stable coexistence equilibria.

Figure 3 shows how the local stability threshold varies with the delayed-product coefficient $\xi$, the two phenotype-conversion rates $\gamma_1$ and $\gamma_2$, and the M2 loss rate $\mu_2$. The corresponding two-parameter stability boundaries in the $(\xi, T)$ plane are displayed in Figure 4; together, these diagrams show that the effect of the memory-kernel shape persists across the considered parameter variations.

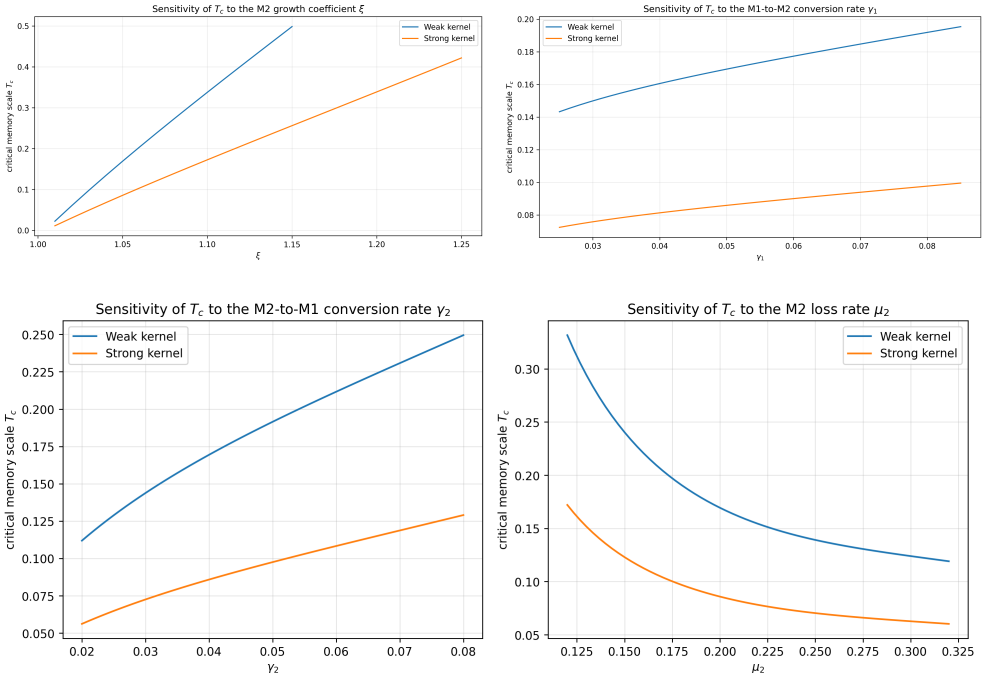


**Figure 3.** Continuation of the local stability threshold $T_c$ with respect to four representative biological parameters, with all non-varied parameters fixed at their Table 1 values. Top row: M2 growth coefficient $\xi$ (left) and M1-to-M2 conversion coefficient $\gamma_1$ (right). Bottom row: M2-to-M1 conversion coefficient $\gamma_2$ (left panel) and M2 loss rate $\mu_2$ (right panel). The curves are computed by direct continuation of the zero-spectral-abscissa boundary of the augmented Jacobians.

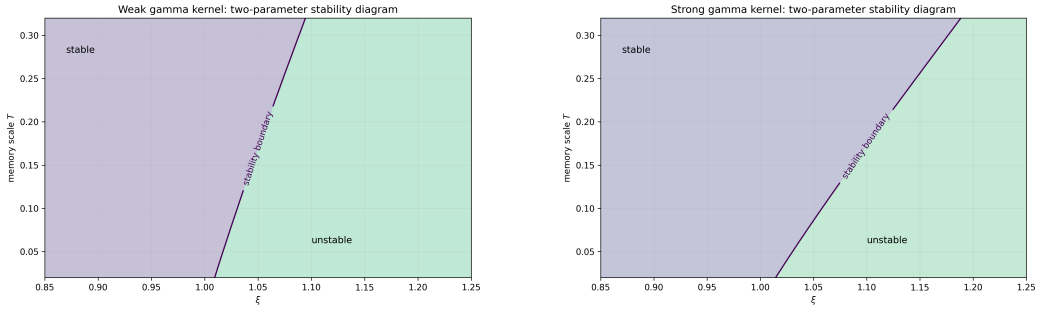


**Figure 4.** Two-parameter local stability diagrams in the $(\xi, T)$ plane. The curves are zero-spectral-abscissa boundaries for the weak (left) and strong (right) gamma kernels.

The representative time series in Figures 5–8 illustrate the four dynamical regimes identified by the spectral analysis. At each value of $T$, the weak and strong kernels are compared side by side. The simulations use the initial condition $(x(0), y(0), z(0)) = (2, 0.2, 0.4)$ of [24] and are consistent with the linear analysis, but do not establish the existence, amplitude, or stability of nonlinear periodic orbits.

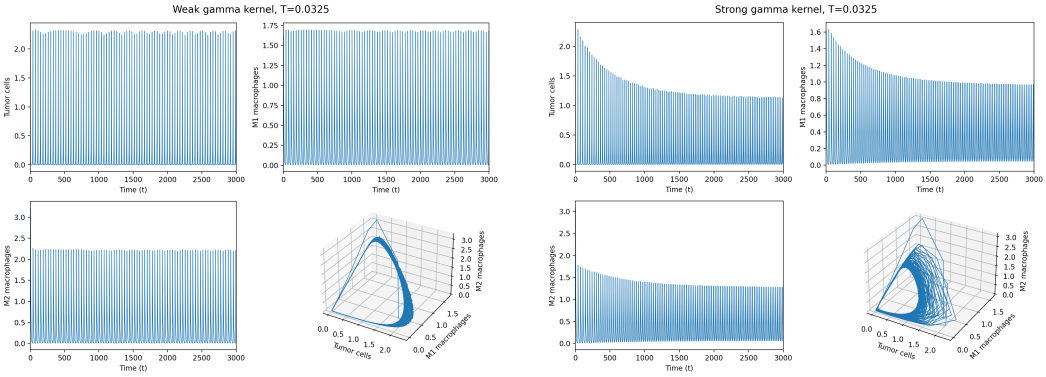


**Figure 5.** Below-threshold regime, $T = 0.0325$. Both kernels lie below their respective thresholds ($T < T_{c,s} < T_{c,w}$): persistent oscillations are observed in both cases, consistent with the positive spectral abscissa in Figure 2. (Left): weak kernel. (Right): strong kernel.

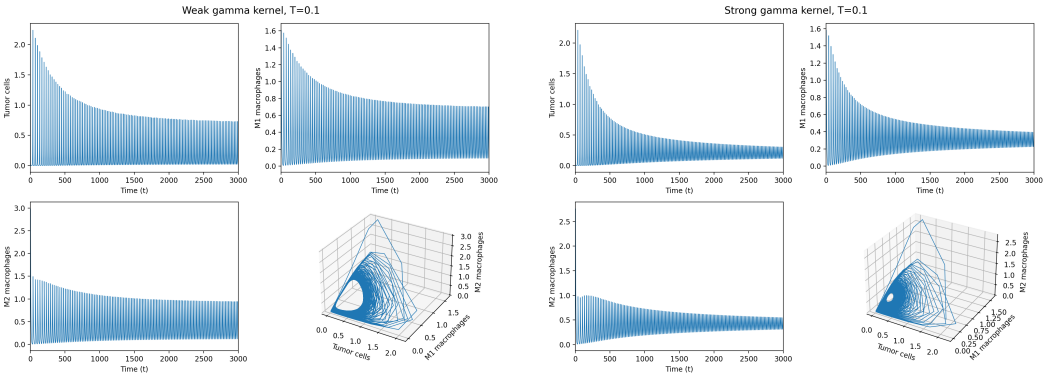


**Figure 6.** Intermediate regime, $T = 0.1$: the kernel-shape-dependent regime gap. The strong kernel (right) has crossed its threshold ($T > T_{c,s} \approx 0.086$) and converges to $E^*$, whereas the weak kernel (left) has not ($T < T_{c,w} \approx 0.169$) and remains oscillatory. This is the clearest evidence that memory shape, not only scale, determines the qualitative outcome.

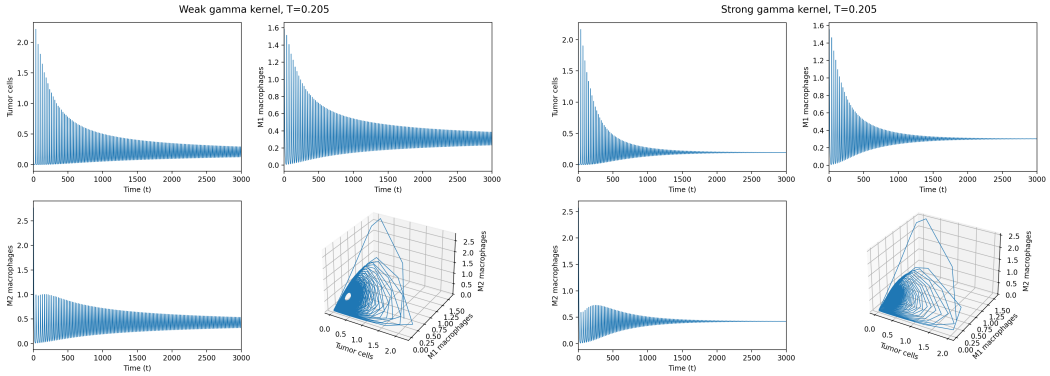


**Figure 7.** Above-threshold regime, $T = 0.205$ (the discrete-delay Hopf value $\theta_c$ of [24]). Both distributed models are now inside the stable region. The weak kernel (left) shows slowly damped oscillations, whereas the strong kernel (right) converges more rapidly, consistently with its deeper placement inside the stable region.

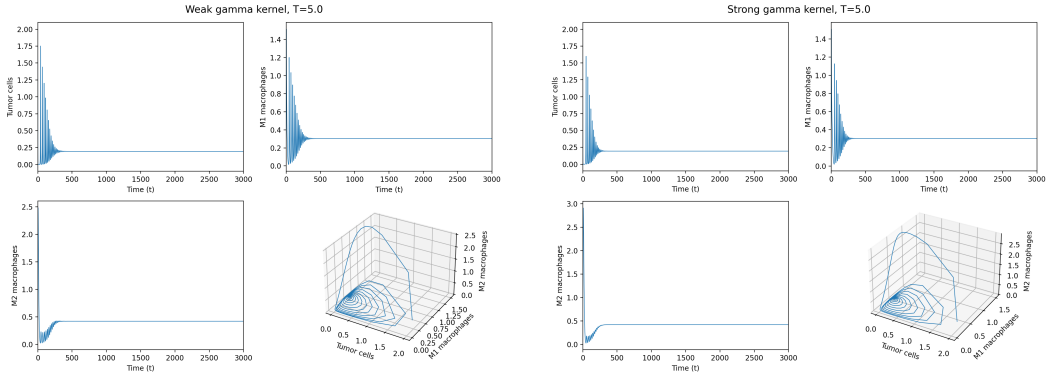


**Figure 8.** Large-memory regime, $T = 5$. Both kernels produce rapid damping and convergence to $E^* = (0.194, 0.304, 0.422)$ within approximately 400 time units. The two solutions are visually indistinguishable, in agreement with the convergent spectral curves in Figure 2 for large $T$.

## 9. Discussion

The discrete-delay model of Dehingia et al. [24] assumes that the delayed contribution to M2 macrophage growth occurs after one fixed time $\theta$. In the characteristic equation this assumption gives the transcendental factor $e^{-\lambda\theta}$. The weak and strong gamma models analyzed here replace this point delay by rational kernel factors. This change is mathematically useful because the linear chain trick transforms the stability problem into a finite-dimensional polynomial problem, which can be addressed with the Routh–Hurwitz criterion in closed form. It is also biologically meaningful because the maturation, activation and transport processes involved in macrophage dynamics are unlikely to occur at exactly the same time for all cells; a distributed lag is therefore a more faithful representation of cellular heterogeneity.

### *9.1. Structural Conclusion: Invariance of Equilibria*

The most important structural conclusion of the analysis is that the equilibria do not change. This follows from the unit mass of the kernels: at equilibrium the past history is constant, and the distributed average of $x^*z^*$ is again $x^*z^*$. Therefore, the tumor-free, the tumor-dominant and the coexistence states coincide with those of the reference model for every $T > 0$. This invariance is biologically informative: it means that the equilibrium "targets" the system can reach (in particular, the coexistence pattern $(0.194, 0.304, 0.422)$ for the parameter set considered) are intrinsic features of the model and do not depend on the

assumed distribution of past times. Only the rate at which these states are approached, and whether they are stable or surrounded by sustained oscillations, depends on the kernel.

### *9.2. Spectral Consequence: Kernel-Dependent Stability*

The stability properties, however, do change because the linearized perturbations are filtered by the memory kernel. For the present parameter set, the weak gamma model stabilizes the coexistence equilibrium at $T_{c,w} \approx 0.1694$, while the strong gamma model stabilizes it at $T_{c,s} \approx 0.0859$; in mean-memory units, both thresholds are very close, approximately 0.1694 and 0.1717. The discrete-delay model stabilizes the same equilibrium at $\theta_c \approx 0.205$. Two messages emerge.

First, the difference between the strong and weak distributed thresholds is essentially a matter of parametrization, not of dynamics: the mean memory at the threshold is virtually the same. The strong kernel has a smaller scale parameter only because the mean of a strong kernel is twice its scale.

Second, both distributed thresholds are visibly smaller than the discrete-delay threshold $\theta_c \approx 0.205$. For the reported parameter set, replacing the fixed-delay factor by a gamma-kernel factor shifts the spectral boundary toward smaller memory values. This is a precise local spectral observation: the relevant characteristic factor changes from $e^{-\lambda\theta}$ to $(1 + T\lambda)^{-n}$, rather than a general claim that distributed memory is intrinsically stabilizing. Figure 2 displays the associated zero crossings of the spectral abscissa.

### *9.3. The Role of Memory Shape: A Qualitative Regime Gap*

A finer message of the present work is that the shape of the memory distribution, not only its scale, can change the qualitative outcome of the model. The clearest evidence is the comparison at $T = 0.1$: both kernels share the same scale parameter, the same total memory mass, the same equilibrium and the same parameter values, yet the strong-kernel model is stable and the weak-kernel model is unstable. The two formulations differ only in whether the memory of past tumor–M2 interactions is concentrated near the present (weak kernel) or around a positive maturation time (strong kernel). The fact that this single qualitative difference is enough to move the system from one side of the Hopf boundary to the other suggests that empirical efforts to identify the relevant memory kernel from biological data are not optional.

In biological terms, the weak kernel models a population in which most pro-tumor M2 macrophages enter their proliferative phase almost immediately after the tumor–M2 interaction occurs, with the remaining individuals contributing exponentially less as the interaction recedes into the past. The strong kernel models a population in which there is a typical maturation delay before any individual responds, with the response distribution peaked at this maturation time and decaying on either side. The latter description is closer to what is known biologically: macrophage polarization, cytokine production and downstream signaling are multi-step processes that do not occur instantaneously, so a kernel that assigns zero weight to $s = 0$ may be a more faithful representation of multi-step polarization kinetics than one that assigns its maximum to $s = 0$, although this conjecture awaits experimental calibration from longitudinal macrophage-polarization data. Within the limits of the present model, this difference translates into a faster stabilization of the coexistence equilibrium.

### *9.4. Comparison with Dehingia et al. [24]*

The comparison with the fixed-delay reference is therefore precise. The two papers share the same model structure, the same equilibria, the same biological interpretation of the delayed term, the same parameter set and the same initial conditions; the only difference is the kernel through which the past acts on the present. The reference paper

located a critical delay near $\theta = 0.205$. For the present parameter set, the distributed kernels produce lower local spectral thresholds, and the amount of memory required to cross the local boundary depends on the kernel shape. Because no nonlinear normal-form calculation is performed, this comparison concerns local spectral thresholds rather than the direction or stability of bifurcating periodic orbits.

From a therapeutic viewpoint, this distinction matters. Interventions on M2 maturation (e.g., pharmacological agents that slow down M2 growth, that change the polarization rate, or that re-polarize M2 into M1) are likely to act on the distribution of maturation times rather than on a single fixed delay. If the relevant memory is closer to a weak kernel, the dose or duration required to stabilize the system may be slightly above the reference $\theta_c$; if it is closer to a strong kernel, the same effect can be obtained with less than half the scale parameter. Conversely, two different therapeutic agents that produce the same mean delay on a heterogeneous population may yield similar local stability thresholds for the reference parameter set, as suggested by the proximity of the weak and strong thresholds in mean-memory units.

## 10. Conclusions

This paper introduced weak and strong gamma distributed delays into a tumor–macrophage interaction model in which the growth of pro-tumor M2 macrophages is delayed. The proposed formulation preserves the biological mechanism of the reference fixed-delay model [24] but replaces a single delayed interaction by a weighted history of tumor–M2 interactions. The weak kernel leads to a four-dimensional linear-chain system and a quartic characteristic equation; the strong kernel leads to a five-dimensional system and a quintic characteristic equation. In both cases the Routh–Hurwitz criterion provides explicit algebraic stability conditions, and the Hopf boundary is identified by the vanishing of the relevant Hurwitz determinant ($\Delta_3$ for the quartic, $\Delta_4$ for the quintic) together with the strict positivity of the remaining determinants.

Three quantitative findings have been established. First, the coexistence equilibrium is invariant: it is the same in the fixed-delay, weak-gamma and strong-gamma models, because all three kernels (including the Dirac mass) have unit mass. Second, the stability threshold is kernel-dependent: for the reference parameter set, $T_{c,w} \approx 0.1694$ and $T_{c,s} \approx 0.0859$, corresponding to a mean memory of $2T_{c,s} \approx 0.1717$. Both distributed-memory thresholds are below the discrete-delay threshold $\theta_c \approx 0.205$. Third, the shape of the memory kernel, not only its scale or its mean, can move the system across the Hopf boundary: at $T = 0.1$ the strong-kernel model is stable while the weak-kernel model is unstable.

The numerical simulations confirm the stability calculation and provide a direct, figure-by-figure comparison with the simulations of [24]. At $T = 0.0325$ both kernels display persistent oscillations (Figure 5); at $T = 0.1$ the strong kernel is stable while the weak kernel is not (Figure 6); at $T = 0.205$ both are stable (Figure 7); and at $T = 5$ both converge rapidly (Figure 8). The intermediate regime $T \approx 0.1$, where the strong and weak models predict opposite long-time behaviors at identical scale parameters, isolates the role of kernel shape.

The main modeling message is that distributed memory is not a minor technical variant of a fixed delay. Even when the equilibrium populations are unchanged, the memory kernel modifies the feedback spectrum and shifts the Hopf transition. From a clinical-modelling perspective, this suggests that empirical calibration of the relevant memory distribution from longitudinal data on macrophage maturation should be regarded as a meaningful step in the validation of tumor–macrophage models, on par with the calibration of point parameters.

Several directions are open for future work. On the modeling side: (i) extending the present analysis to phase-type or Erlang-$k$ kernels of order higher than two, in or-

der to cover the entire family of gamma distributions and quantify the dependence of $T_c$ on the kernel order; (ii) introducing state-dependent kernels in which the macrophage maturation distribution depends on local cytokine concentrations or on the proportion of M1 cells; (iii) coupling the distributed-delay framework with therapy terms such as M2 re-polarization [9], dendritic cell vaccines or chemotherapy, in order to test how pharmacological interventions modify the threshold $T_c$. On the mathematical side, the next steps are: (a) computing the first Lyapunov coefficient at the Hopf points to classify the bifurcating periodic orbits as super- or subcritical; (b) designing feedback or delay-based control strategies to shift or suppress the Hopf threshold, in the spirit of bifurcation control [46,47]; (c) extending the present analysis to a global setting via Lyapunov functionals or persistence theory; (d) coupling the distributed memory with spatial mechanisms (diffusion, chemotaxis) along the lines of [11,13] in order to study how memory and spatial structure interact in shaping the tumor–macrophage system. Fractional-order generalizations of delayed biological models [46,47] offer a further avenue, although the present analysis is restricted to integer-order dynamics.

**Author Contributions:** Conceptualization, C.B., L.G. and S.R.; Methodology, C.B., L.G. and S.R.; Formal Analysis, C.B., L.G. and S.R.; Investigation, C.B., L.G. and S.R.; Writing—Original Draft Preparation, C.B., L.G. and S.R.; Writing—Review and Editing, C.B., L.G. and S.R. All authors have read and agreed to the published version of the manuscript.

**Funding:** This research received no external funding.

**Data Availability Statement:** The original contributions presented in this study are included in the article. Further inquiries can be directed to the corresponding author.

**Acknowledgments:** The authors sincerely thank the anonymous referees for their careful reading and constructive suggestions, which substantially improved the presentation of this work.

**Conflicts of Interest:** The authors declare no conflicts of interest.

## References

1. Shu, Y.; Huang, J.; Dong, Y.; Takeuchi, Y. Mathematical modeling and bifurcation analysis of pro- and anti-tumor macrophages. *Appl. Math. Model.* **2020**, *88*, 758–773. [CrossRef]
2. Khajanchi, S.; Perc, M.; Ghosh, D. The influence of time delay in a chaotic cancer model. *Chaos* **2018**, *28*, 103101. [CrossRef] [PubMed]
3. Dehingia, K.; Sarmah, H.K.; Alharbi, Y.; Hosseini, K. Mathematical analysis of a cancer model with time-delay in tumor–immune interaction and stimulation processes. *Adv. Differ. Equ.* **2021**, *2021*, 473. [PubMed]
4. Dong, Y.; Miyazaki, R.; Huang, G.; Takeuchi, Y. Dynamics in a tumor immune system with time delays. *Appl. Math. Comput.* **2015**, *252*, 99–113. [CrossRef]
5. Mantovani, A.; Schioppa, T.; Porta, C.; Allavena, P.; Sica, A. Role of tumor-associated macrophages in tumor progression and invasion. *Cancer Metastasis Rev.* **2006**, *25*, 315–322. [CrossRef] [PubMed]
6. den Breems, N.Y.; Eftimie, R. The re-polarisation of M2 and M1 macrophages and its role on cancer outcomes. *J. Theor. Biol.* **2016**, *390*, 23–39. [CrossRef] [PubMed]
7. Pan, Y.; Yu, Y.; Wang, X.; Zhang, T. Tumor-associated macrophages in tumor immunity. *Front. Immunol.* **2020**, *11*, 583084. [CrossRef] [PubMed]
8. Shojaee, P.; Mornata, F.; Deutsch, A.; Locati, M.; Hatzikirou, H. The impact of tumor-associated macrophages on tumor biology under the lens of mathematical modelling: A review. *Front. Immunol.* **2022**, *13*, 1050067. [PubMed]
9. Guo, Y.; Fan, L.; Wang, X. Mathematical investigation of the role of re-polarisation of M2 in cancer therapy. *Discrete Contin. Dyn. Syst. Ser. B* **2023**, *28*, 2718–2744. [CrossRef]
10. Li, J.; Liu, N.; Wang, D.; Yang, H. Mathematical modeling and Hopf bifurcation analysis of tumor macrophage interaction with polarization delay. *J. Biol. Dyn.* **2025**, *19*, 2508240. [CrossRef] [PubMed]
11. Lampropoulos, I.; Kevrekidis, P.G.; Zois, C.E.; Byrne, H.; Kavousanakis, M. Spatio-temporal dynamics of M1 and M2 macrophages in a multiphase model of tumor growth. *Bull. Math. Biol.* **2025**, *87*, 92. [CrossRef] [PubMed]

12. Morgado, G.; Lemarchand, A.; Bianca, C. From cell–cell interaction to stochastic and deterministic descriptions of a cancer–immune system competition model. *Mathematics* **2023**, *11*, 2188.
13. Conte, M.; Travaglini, R. A kinetic derivation of spatial distributed models for tumor–immune system interactions. *Chaos Solitons Fractals* **2025**, *200*, 116969.
14. Khajanchi, S.; Nieto, J.J. Mathematical modeling of tumor–immune competitive system, considering the role of time delay. *Appl. Math. Comput.* **2019**, *340*, 180–205.
15. Sardar, M.; Khajanchi, S.; Biswas, S.; Abdelwahab, S.F.; Nisar, K.S. Exploring the dynamics of a tumor–immune interplay with time delay. *Alex. Eng. J.* **2021**, *60*, 4875–4888.
16. Sardar, M.; Biswas, S.; Khajanchi, S. The impact of distributed time delay in a tumor–immune interaction system. *Chaos Solitons Fractals* **2021**, *142*, 110483.
17. Tang, Q.; Zhang, G. Stability and Hopf bifurcations in a competitive tumour–immune system with intrinsic recruitment delay and chemotherapy. *Math. Biosci. Eng.* **2021**, *18*, 1941–1965. [PubMed]
18. Yang, Y.; Fu, S. Hopf bifurcation of a tumor immune model with time delay. *Front. Math. China* **2022**, *17*, 315–335. [CrossRef]
19. Sardar, M.; Khajanchi, S.; Biswas, S.; Ghosh, S. A mathematical model for tumor–immune competitive system with multiple time delays. *Chaos Solitons Fractals* **2024**, *179*, 114397.
20. Bastian, F.; Alkhayuon, H.; Mulchrone, K.; O'Riordain, M.; Wieczorek, S. Cancer model with moving extinction threshold reproduces real cancer data. *J. R. Soc. Interface* **2025**, *22*, 20240844. [CrossRef] [PubMed]
21. Li, J.; Ma, X.; Chen, Y.; Zhang, D. Complex dynamic behaviors of a tumor–immune system with two delays in tumor actions. *Discrete Contin. Dyn. Syst. Ser. B* **2022**, *27*, 7065–7087.
22. Ding, Y.; Liu, G.; An, Y. Stability and bifurcation analysis of a tumor–immune system with two delays and diffusion. *Math. Biosci. Eng.* **2022**, *19*, 1154–1173. [PubMed]
23. Zhang, Y.; Xie, L.; Dong, Y.; Huang, J.; Ruan, S.; Takeuchi, Y. Bifurcation analysis in a tumor–immune system interaction model with dendritic cell therapy and immune response delay. *SIAM J. Appl. Math.* **2023**, *83*, 1892–1914.
24. Dehingia, K.; Hosseini, K.; Salahshour, S.; Baleanu, D. A detailed study on a tumor model with delayed growth of pro-tumor macrophages. *Int. J. Appl. Comput. Math.* **2022**, *8*, 245. [CrossRef]
25. Das, A.; Dehingia, K.; Sarmah, H.K.; Hosseini, K.; Sadri, K.; Salahshour, S. Analysis of a delay-induced mathematical model of cancer. *Adv. Contin. Discrete Models* **2022**, *2022*, 15. [CrossRef]
26. Hurtado, P.J.; Kirosingh, A.S. Generalizations of the linear chain trick: Incorporating more flexible dwell time distributions into mean field ODE models. *J. Math. Biol.* **2019**, *79*, 1831–1883. [CrossRef] [PubMed]
27. Cassidy, T. Distributed delay differential equation representations of cyclic differential equations. *SIAM J. Appl. Math.* **2021**, *81*, 1742–1766. [CrossRef]
28. Cassidy, T.; Gillich, P.; Humphries, A.R.; van Dorp, C.H.T. Numerical methods and hypoexponential approximations for gamma distributed delay differential equations. *IMA J. Appl. Math.* **2022**, *87*, 1043–1089. [CrossRef] [PubMed]
29. Mielke, A.; Sørensen, M.P.; Wyller, J. Memory effects in disease modelling through kernel estimates with oscillatory time history. *J. Math. Biol.* **2024**, *88*, 57. [CrossRef] [PubMed]
30. Andò, A.; Breda, D.; Gava, G. How fast is the linear chain trick? A rigorous analysis in the context of behavioural epidemiology. *Math. Biosci. Eng.* **2020**, *17*, 5059–5084. [PubMed]
31. Al-Darabsah, I. On the stability of a single-species model with a generic delay distribution kernel. *Chaos Solitons Fractals* **2024**, *187*, 115425. [CrossRef]
32. Glass, D.S.; Jin, X.; Riedel-Kruse, I.H. Nonlinear delay differential equations and their application to modeling biological network motifs. *Nat. Commun.* **2021**, *12*, 1788. [CrossRef] [PubMed]
33. Padder, A.; Matouk, A.E.; Qureshi, S.; Dehingia, K.; Shah, T.U.R. Analyzing the impact of single feedback control strategy on the dynamics of fractional order tumor model. *Discov. Appl. Sci.* **2025**, *7*, 1301. [CrossRef]
34. Antonopoulos, C.G.; Akrami, M.H.; Basios, V.; Latifi, A. A generic model for pandemics in networks of communities and the role of vaccination. *Chaos* **2022**, *32*, 063127. [CrossRef] [PubMed]
35. MacDonald, N. *Time Lags in Biological Models*; Springer: Berlin, Germany, 1978.
36. Cushing, J.M. *Integro-Differential Equations and Delay Models in Population Dynamics*; Springer: Berlin, Germany, 1977.
37. Kuang, Y. *Delay Differential Equations with Applications in Population Dynamics*; Academic Press: Boston, MA, USA, 1993.
38. Hale, J.K.; Verduyn Lunel, S.M. *Introduction to Functional Differential Equations*; Springer: New York, NY, USA, 1993.
39. Smith, H. *An Introduction to Delay Differential Equations with Applications to the Life Sciences*; Springer: New York, NY, USA, 2011.
40. Ruan, S. Delay differential equations in single species dynamics. In *Delay Differential Equations and Applications*; Springer: Dordrecht, The Netherlands, 2006; pp. 477–517.
41. Bellman, R.; Cooke, K.L. *Differential–Difference Equations*; Academic Press: New York, NY, USA, 1963.
42. Hassard, B.D.; Kazarinoff, N.D.; Wan, Y.H. *Theory and Applications of Hopf Bifurcation*; Cambridge University Press: Cambridge, UK, 1981.

43. Khajanchi, S.; Bera, S.; Roy, T.K. Mathematical analysis of the global dynamics of a HTLV-I infection model, considering the role of cytotoxic T-lymphocytes. *Math. Comput. Simul.* **2021**, *180*, 354–378. [CrossRef]
44. Kirschner, D.; Panetta, J.C. Modeling immunotherapy of the tumor–immune interaction. *J. Math. Biol.* **1998**, *37*, 235–252. [CrossRef] [PubMed]
45. Liu, W.M. Criterion of Hopf bifurcations without using eigenvalues. *J. Math. Anal. Appl.* **1994**, *182*, 250–256. [CrossRef]
46. Xu, C.; Aouiti, C.; Liu, Z.; Li, P.; Yao, L. Adaptive Fault-Tolerant control for consensus of nonlinear Fractional-Order Multi-Agent systems with diffusion. *Fractal Fract.* **2023**, *7*, 760.
47. Shu, X.; Xu, C.; Cao, X. Hunting cooperation and gestation delay in a prey–predator model with fractional derivative. *J. Appl. Anal. Comput.* **2026**, *16*, 1035–1053.